doi:10.1016/j.jmb.2004.09.067 J. Mol. Biol. (2004) xx, 1–18

JMB

Available online at www.sciencedirect.com

SCIENCE DIRECT®

ELSEVIER

Acid-induced Unfolding of the Amino-terminal Domains of the Lethal and Edema Factors of Anthrax Toxin

Bryan A. Krantz, Amar D. Trivedi, Kristina Cunningham Kenneth A. Christensen and R. John Collier*

Department of Microbiology and Molecular Genetics Harvard Medical School, 200 Longwood Ave., Boston, MA 02115, USA

*Corresponding author

The two enzymatic components of anthrax toxin, lethal factor (LF) and edema factor (EF), are transported to the cytosol of mammalian cells by the third component, protective antigen (PA). A heptameric form of PA binds LF and/or EF and, under the acidic conditions encountered in endosomes, generates a membrane-spanning pore that is thought to serve as a passageway for these enzymes to enter the cytosol. The pore contains a 14-stranded transmembrane β-barrel that is too narrow to accommodate a fully folded protein, necessitating that LF and EF unfold, at least partly, in order to pass. Here, we describe the pH-dependence of the unfolding of LF_N and EF_N, the 30 kDa N-terminal PA-binding domains, and minimal translocatable units, of LF and EF. Equilibrium chemical denaturation studies using fluorescence and circular dichroism spectroscopy show that each protein unfolds *via* a four-state mechanism: N↔I↔J↔U. The acid-induced N→I transition occurs within the pH range of the endosome (pH 5–6). The I state predominates at lower pH values, and the J and U states are populated significantly only in the presence of denaturant. The I state is compact and has characteristics of a molten globule, as shown by its retention of significant secondary structure and its ability to bind an apolar fluorophore. The N→I transition leads to an overall 60% increase in buried surface area exposure. The J state is expanded significantly and has diminished secondary structure content. We analyze the different protonation states of LF_N and EF_N in terms of a linked equilibrium proton binding model and discuss the implications of our findings for the mechanism of acidic pH-induced translocation of anthrax toxin. Finally, analysis of the structure of the transmembrane β-barrel of PA shows that it can accommodate α-helix, and we suggest that the steric constraints and composition of the lumen may promote α-helix formation.

Keywords: anthrax toxin; lethal factor; edema factor; translocation; unfolding pathway

Introduction

The pathology of *Bacillus anthracis* is due, in part, to the production of a toxin, an ensemble of three non-toxic monomeric proteins that combine at the surface of host cells to form toxic non-covalent complexes (Figure 1A). Two of these are enzymes that modify cytosolic substrates: lethal factor (LF; 90 kDa) is a Zn^{2+} protease that cleaves several mitogen-activated protein kinase kinases;[1,2] and edema factor (EF; 89 kDa) is a Ca^{2+} and calmodulin-dependent adenylate cyclase.[3] The third, protective antigen (PA_{83}; 83 kDa), binds to cellular receptors and transports LF and EF to the cytosol.

The initial step in the action of anthrax toxin

Abbreviations used: AF488, Alexa Fluor 488; AF546, Alexa Fluor 546; ASA, solvent-accessible surface area; bis-ANS, 4,4′-dianilino-1,1′-binaphthyl-5,5′-disulfonic acid; EF, edema factor; EF_N, edema factor's amino-terminal domain (residues 1–254); EF_N*, EF_N with a AF488/AF546 FRET pair; Fl, fluorescence; FRET, fluorescence resonance energy transfer; GdmCl, guanidinium chloride; LF, lethal factor; LF_N, lethal factor's amino-terminal domain (residues 1–263); LF_N*, LFN with an AF488/AF546 FRET pair; MG, molten globule; PA, protective antigen; β_{eq}, relative surface area buried in an equilibrium transition computed from *m*-values; $\Delta\Delta G^{H+}$, equilibrium folding free energy change due to the protonation; ϕ_{eq}^{H+}, percentage of protonation free energy change realized in an equilibrium folding transition.

E-mail address of the corresponding author: jcollier@hms.harvard.edu

0022-2836/$ - see front matter

(Figure 1A) is binding of protective antigen (PA) to a von Willebrand A domain of a cell-surface receptor.[4,5] Receptor-bound PA is cleaved into two fragments by a furin-family protease.[6] Dissociation of the smaller fragment allows the larger, receptor-bound fragment to self-associate into a ring shaped heptamer, referred to as the PA_7 prepore.[7] The PA_7 prepore may bind up to three molecules of LF and/or EF[8] with tight affinity.[9] The resulting complexes are endocytosed and delivered to an acidic compartment,[10] where PA_7 is converted from the prepore state to an integral membrane, ion-conductive pore.[11] The process of translocating LF and EF into the cytosol is linked to the formation of a pore, but the nature of this relationship is poorly understood. Within the cytosol these enzymatically active moieties may then disrupt normal cellular physiology.

Heretofore, studies of anthrax toxin's mechanism of translocation have been focused mainly on the dramatic conformational changes occurring in PA_7 upon acidification,[11,12] and no study has addressed the acid-induced changes in the individual *A* moieties, LF and EF. PA_7's prepore structure revealed that the central lumen is too small to accommodate native LF or EF,[13] necessitating some degree of protein unfolding for efficient translocation. In accordance with this idea, disulfide-stabilized and liganded protein fusions of LF_N with either diphtheria toxin A domain or dihydrofolate reductase have reduced translocation efficiency significantly.[14] Thus, stabilized toxin fusions suppress an unfolding event that is required for translocation of EF and LF.

Here, we focus on the pH-dependence of the equilibrium folding stability of LF and EF's highly homologous ~250 residue amino-terminal domains (LF_N and EF_N). These domains share 35% sequence identity;[15] and a threading algorithm[16] predicts that EF_N's fold mirrors that of LF_N (Figure 1B).[17] These domains are necessary and sufficient for binding to PA_7 and are able to undergo PA_7-mediated translocation into the host's cytosol. Furthermore, fusing LF_N to some, but not all, heterologous proteins was shown to potentiate them for PA_7-mediated translocation.[14]

By fluorescence and circular dichroism (CD) spectroscopy, LF_N and EF_N unfold *via* a four-state mechanism. The native-to-intermediate transition is destabilized upon reduction in pH, leading to significant population of a "molten globule" (MG) intermediate.[18–21] This acid-induced MG unfolding mechanism was previously hypothesized[22] and experimentally determined to be crucial to the translocation of some other bacterial toxins across cellular membranes.[23–26] Endosomal acidification may destabilize proteins that are stable and folded at neutral pH, allowing them to translocate into the host's cell in the absence of ATP-driven cellular factors commonly required to facilitate unfolding. This translocation pathway, in the case of anthrax toxin, depends on the formation of a 14-stranded β-barrel molecular tube[27,28] (akin to that formed by staphylococcal α-hemolysin)[29] that chaperones the acid-destabilized moieties, LF and EF, across membranes. Because a disproportionate amount of secondary structure remains intact in the MG, we model whether residual secondary structure is compatible with the dimensions of PA pore's membrane-spanning molecular tube. Even the bulkiest secondary structure, α-helix, is shown to be accommodated by PA's lumen, making such residual structure less of a factor than anticipated.

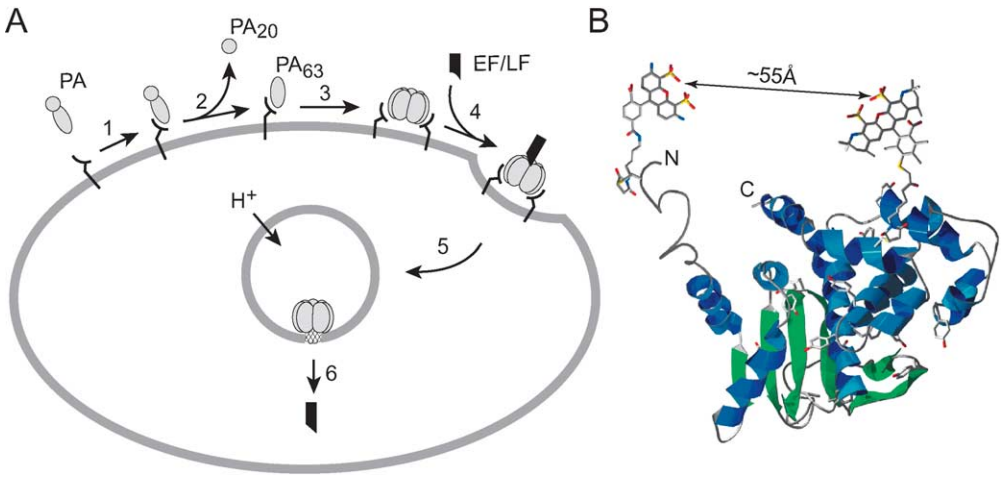

Figure 1. A, Model of anthrax toxin entry into cells: 1, Binding of PA_{83} to its cellular receptor; 2, proteolytic activation of PA and dissociation of PA_{20}; 3, self-association of monomeric PA_{63} to form the heptameric prepore, PA_7; 4, binding of EF/LF to PA_7; 5, endocytosis of the receptor/PA_7/ligand complex; 6, acid-induced insertion of PA_{63} and translocation of EF and LF. B, Structure of LF_N, residues 27–263 of LF[17] with a modeled amino terminus: α-helix (blue; 42%), β-sheet (green; 13%), and loop/coil (gray; 46%). FRET dyes, AF488 and AF546, are attached at residues 14 and 242, respectively. All 14 native Tyr residues are depicted.

Results

Derivatization of LF_N and EF_N with fluorescent dyes

The constructs used,[15] based on the structure of LF,[17] were engineered by site-directed mutagenesis to have two Cys residues, introduced near their amino and carboxy termini. These sites are expected to be within 40–60 Å in the folded form (Figure 1B). Two differently colored, maleimide-reactive fluorophores were coupled to the dual-Cys proteins using a multi-step procedure. First, a stoichiometric equivalent of Alexa Fluor 488 C_5 maleimide (AF488) was reacted with the protein, and the reaction mixture was fractionated by anion-exchange chromatography. A peak containing a single equivalent of AF488 per protein was then reacted with an excess of the second fluorophore, Alexa Fluor 546 C_5 maleimide (AF546), and the dual-labeled product was purified. The final preparations, referred to as LF_N^* and EF_N^*, contain between ~0.8 and 1.2 eq of each dye.

Fluorescence resonance energy transfer (FRET) characterization of LF_N^* and EF_N^*.

Knowing the relationship, $E(R) = R_o^6/(R_o^6 + r^6)$ and the ~60 Å Förster distance, R_o, for the two Alexa Fluor dyes, we determined the FRET distance, r, for LF_N^* and EF_N^*, using a ratiometric protocol.[30] FRET efficiencies, E, generated r values for native LF_N^* and EF_N^* of 55(±2) Å and 53(±3) Å, respectively (pH 6–9). Measurement integrity depends strictly on how uniformly a protein preparation is labeled with a single donor and acceptor; however, r is consistent with the crystal structure,[17] considering the lack of ordered structure in LF_N's amino terminus (first 27 residues) and the long C_5 linkers on each fluorophore. Finally, the addition of high concentrations of guanidinium chloride (GdmCl) eliminated FRET in LF_N^*; sensitized emission of the acceptor decreased while donor intensity increased, indicating expansion in the inter-fluorophore distance far beyond R_o (Figure 2A).

Analysis of small-angle X-ray-scattering studies of proteins denatured by chemical denaturants[31] estimates that the radius of gyration (R_g) of denatured LF_N (~250 residues) should be ~53 Å. From an ideal relationship between the root-mean-squared end-to-end distance ($r_{end\text{-}to\text{-}end}$) and R_g, $\langle R_g \rangle^2 = \langle r_{end\text{-}to\text{-}end} \rangle^2/6$, the predicted inter-fluorophore distance in 6 M GdmCl denaturant is ~130 Å. Our estimates of r for the unfolded state (U) in 6 M GdmCl show that it is >110 Å and beyond the limit of the FRET pair's useful range, indicating, therefore, that U approximates an ideal random-flight chain.

FRET equilibrium denaturation profiles are four-state

We then probed the equilibrium denaturation profiles of LF_N^* and EF_N^* using the ratio of the 570 nm and 520 nm band intensities to report denaturation. At neutral to high pH values, the GdmCl profiles could not be fit adequately to either

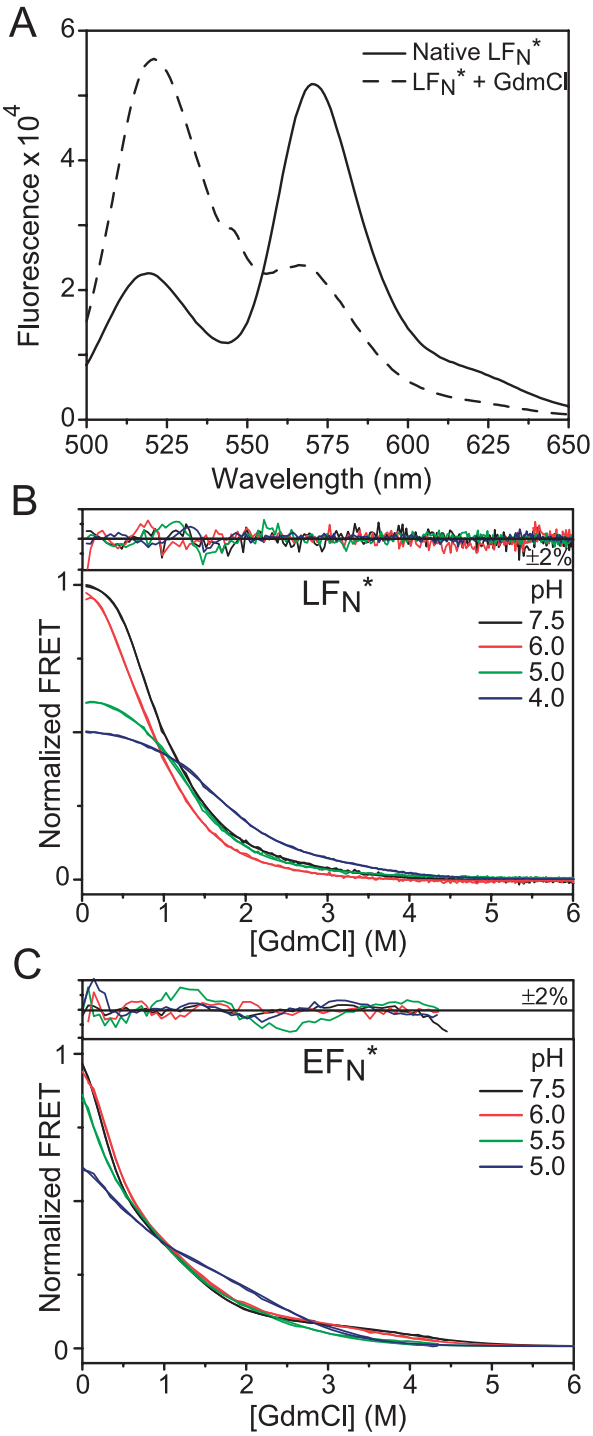

Figure 2. FRET spectra and denaturation profiles. A, Fluorescence spectra of LF_N^* (excitation by 488 nm Ar^+ line) in the absence (continuous line) and presence (broken line) of 3 M GdmCl, pH 8. FRET GdmCl profiles at 20 °C for (B) LF_N^* and (C) EF_N^* at different pH values. Signals (ratio of intensity at 520 nm and 570(±16) nm) are fit to a four-state model. Fit parameters are shown in Figure 6. Profiles are normalized such that θ_U for either protein is defined as zero and θ_N is unity.

a two-state or a three-state equilibrium denaturation model without significant systematic deviations in the residuals. Rather, they are best fit by a four-state model, N↔I↔J↔U (Figure 2B and C; Materials and Methods). Here, two intermediate forms, states I and J, are populated, as the native state, N, was denatured to the fully unfolded form, U. The standard free energies, ΔG, for each of the three transitions, N→I, I→J, J→U, are calculated in the absence of denaturant and are compiled in Figure 6.

To corroborate the four-state thermodynamic model, we examined the denaturant-dependence of the free energy changes, or *m*-values.[32,33] The *m*-values, which report on the amount of denaturant-sensitive surface area exposed during an unfolding transition, are ~3.6 kcal mol^{-1} M^{-1}, 1.4 kcal mol^{-1} M^{-1} and 1.1 kcal mol^{-1} M^{-1} for m_{NI}, m_{IJ} and m_{JU}, respectively (Table 1), totaling ~6 kcal mol^{-1} M^{-1} for the N→U transition (1 cal=4.184 J). The expected value calculated for a 263 residue protein is 6.0 kcal mol^{-1} M^{-1}or 5.6 kcal mol^{-1} M^{-1}, depending on whether surface area is estimated by LF_N's number of residues or its structure.[17,34,35] Nonetheless, when two-state and three-state curve fits are applied, the resulting total m_{NU} values of 1.5 kcal mol^{-1} M^{-1} and 2.4 kcal mol^{-1} M^{-1}, respectively, are significantly less than expected.

We also calculated FRET distances, *r*, from pH 7–10 using the individual signal amplitudes, θ_I and θ_J, of the intermediates, I and J (Materials and Methods). Here, we assume, to a first approximation, that the FRET efficiency is zero in the unfolded state and use the native state's *r* values estimated above. Therefore, the FRET distances for states I and J are 59(±3) Å and 103(±5) Å, respectively, for LF_N^* and 67.6(±0.2) Å and 97(±5) Å, respectively, for EF_N^*.

While free energies defining the transitions' stabilities (ΔG_{NI}, ΔG_{IJ} and ΔG_{JU}) are generally unaffected at neutral to mildly basic pH values, ΔG_{NI}, ΔG_{IJ} and ΔG_{JU} are destabilized to various degrees from pH 7 to 5.5. ΔG_{NI} is most destabilized followed by ΔG_{JU}, while ΔG_{IJ} is destabilized only subtly. As the pH is lowered from 5.5 to 3.5, ΔG_{NI} continues to destabilize such that N is no longer detectable, while ΔG_{IJ} and ΔG_{JU} stabilize significantly.

Tyr fluorescence GdmCl profiles

LF_N and EF_N have no tryptophan residue, but have many tyrosine residues (14 and ten, respectively; Figure 1B). Fluorescence (Fl) spectra of GdmCl denatured LF_N in 5 M GdmCl show that U is quenched relative to N (Figure 3A). At neutral to mildly basic pH values, GdmCl profiles recapitulate the four-state mechanism. We observed that LF_N's I state is hypochromic relative to N (36(±10) % quenched), whereas EF_N's I state is hyperchromic relative to N (28(±7) % de-quenched; see also Figure 5A). For LF_N, the relative signal level changes for N→I, I→J, and J→U are remarkably well resolved, as −36(±10) %, −37(±11) %, and −27(±2) %, respectively, of the total N→U signal change from pH 6.5 to 8.5 (Figure 3B). EF_N's relative signal changes for N→I, I→J, and J→U are also well resolved, as +28(±7) %, −107(±5) %, and −21(±2) %, respectively, where the positive percentage change in the N→I signal change indicates a hyperchromic shift (Figure 3C). For either protein, the J state is hyperchromic relative to U, representing ~25% of the total N→U signal change. Observed hyperchromicity in EF_N's N→I transition *versus* LF_N's hypochromicity may be explained by the environments of three non-conserved Tyr residues' phenol side-chains in LF_N (residues 108, 118, and 120) that are largely buried (or 30%, 15%, and 8% solvent-exposed, respectively). These residues may be disrupted in I, thereby explaining the change in sign of the signal change for the two proteins. Tyr Fl and FRET denaturation profiles could be fit simultaneously at a given pH using shared ΔG and *m*-value parameters, showing that the two probes report consistent pH-dependent stability changes (Figure 6).

Far-UV CD

To confirm the four-state model and assess the secondary structure content of the four states, far-UV CD spectra were recorded from pH 2–8 for LF_N and EF_N in the absence of denaturant (Figure 4A and B). The secondary structure content of LF_N as judged by its structure (Figure 1B)[17] is 42% α-helix, 13% β-sheet, and 46% random coil. Spectra at pH 8 for LF_N and EF_N estimate the molar

Table 1. Equilibrium stabilities and *m*-values

Protein	Transition	ΔG° (kcal mol^{-1})	*m* (kcal mol^{-1} M^{-1})
LF_N	N→I	−2.55±0.01 (−2.57±0.01)	3.59±0.05
	I→J	−1.52±0.01 (−1.52±0.01)	1.37±0.03
	J→U	−3.63±0.02 (−3.66±0.01)	1.05±0.05
	N→U	−7.70±0.02 (−7.75±0.02)	6.01±0.08
EF_N	N→I	−1.04±0.01	3.67±0.09
	I→J	−1.80±0.01	1.44±0.03
	J→U	−4.13±0.02	1.19±0.04
	N→U	−7.00±0.02	6.3±0.1

ΔG°, the equilibrium stability in the absence of denaturant at pH ≫ p*K*, is calculated from the data in Figure 6 by equation (3). Values in parentheses for LF_N are from fits using fixed p*K* values for the unfolded state (Table 2). The *m*-values for the N→I transition are obtained by globally fitting all denaturation profiles from ~pH 6–9; *m*-values for the I→J and J→U transitions are obtained using all the available data.

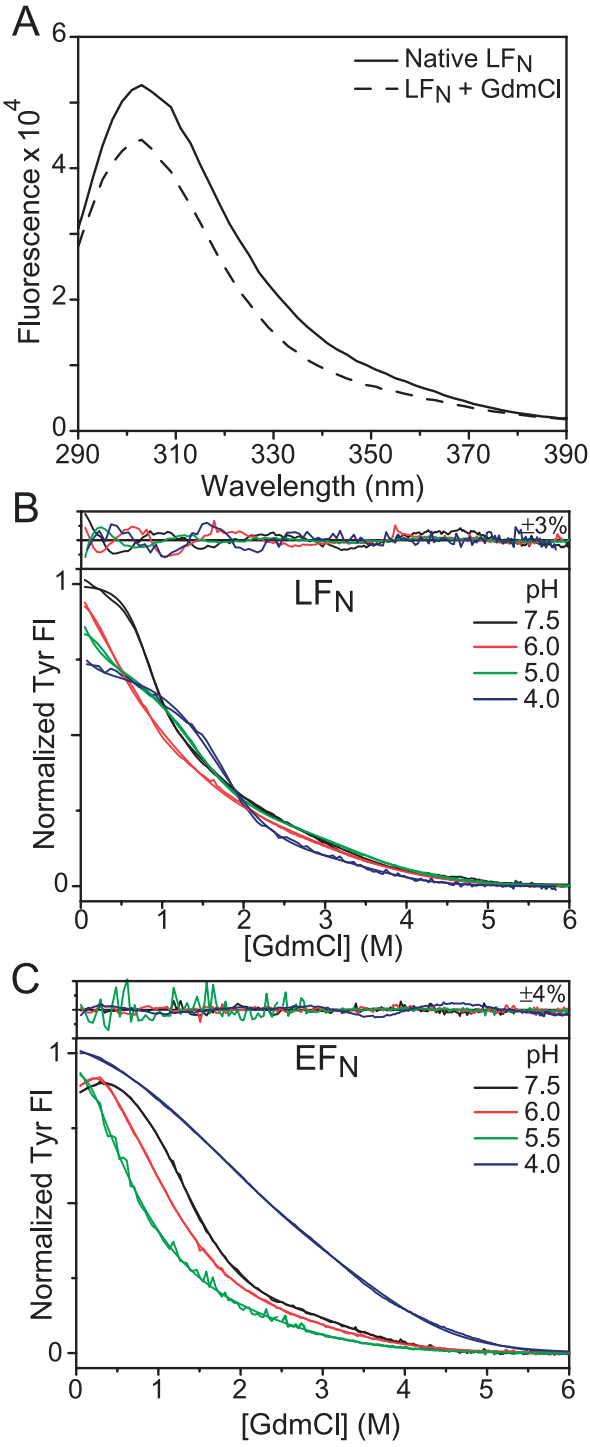

Figure 3. Tyr fluorescence spectra and denaturation profiles. A, Native Tyr Fl at pH 7.5 (excitation 275(±8) nm; continuous line) reports on denaturation by 5 M GdmCl (broken line) as a reduction in intensity. Representative Tyr Fl GdmCl profiles at 20 °C for (B) LF_N and (C) EF_N at different pH conditions (excitation 275(±8) nm; emission 320–340 nm) are fit to four-state models. Fit parameters are shown in Figure 6. θ_U for either protein is defined as zero. θ_N for LF_N, which has a hypochromic θ_I, is normalized to unity, whereas the hyperchromic θ_I for EF_N is normalized to unity.

ellipticities at 222 nm as −8600 and −9600 deg cm^2 dmol^{-1}, respectively. The smaller molar ellipticity determined for LF_N relative to EF_N may reflect the fact that LF_N contains about ten more unstructured residues than EF_N on its N terminus. These molar ellipticities are slightly lower than predicted using Wetlaufer basis spectra,[36] but each protein contains a 21 residue N-terminal His_6 tag that is expected to be "random coil". Furthermore, the first ~27 residues on the N terminus of native LF_N (~17 residues of EF_N by homology) are either disordered or not present in the X-ray crystal structure.[17] When including the His-tag leader, the predicted molar ellipticity at 222 nm for LF_N is −10,600 deg cm^2 dmol^{-1}. Upon further acidification, LF_N loses <10% of its secondary structure as determined by CD at 222 nm, while EF_N loses ~25% of its structure.

ΔG and m-value parameters from denaturation profiles monitored by CD at 222 nm (Figure 4C and D) agree with fluorescence measurements (Figure 6). For either protein, ΔG_{NI} is destabilized dramatically as the pH is lowered from 8 to 5. By pH 2, the N→I transition is undetectable. Average signal changes in the profiles at pH 5 and 8 for LF_N are −22(±11) %, −61(±13) % and −17(±2) % of the total molar ellipticity for the N→I, I→J, and J→U transitions, respectively. Corresponding CD signal changes for EF_N are −19(±2) %, −69.3(±0.4) % and −12(±2) %. For either protein, the I→J transition maintains the largest percentage change in secondary structure. J states consistently retain some residual secondary structure content, ~10–20% of N, while U had no detectable ellipticity.

Tyr fluorescence H^+ titrations

To corroborate the observed acid-induced destabilization of the native state, H^+ titrations were performed in the absence of denaturant. pH was monitored continuously using a microelectrode (Figure 5A). From pH 8 to 5.5, LF_N and EF_N demonstrate their respective characteristic hypochromic and hyperchromic shifts as N depopulates and I populates. These intensity shifts are consistent with denaturation profiles in this pH range (Figure 3B and C). As stated above, the change in intensity may reflect the differing environments of non-conserved Tyr residues, which are buried in the N state but are more exposed in the I state. Alternatively, non-conserved Tyr residues may be quenched differentially in the I state by neighboring weakly basic side-chains from His,[37] Asp and Glu[38] residues or acetate buffer,[38] because weak base carboxylate groups are known to quench by interacting with the excited s1 states of Tyr by weak base-catalyzed deprotonation of the phenol, creating less fluorescent tyrosinates.[37,38] Furthermore, LF_N and EF_N's Tyr fluorescence intensity increases sharply below ~pH 5.4, which is near the pK_a range, 4.2–5.3, expected for tyrosinate.[37–39] This Tyr fluorescence quenching mechanism implies that large-scale conformational fluctuations and

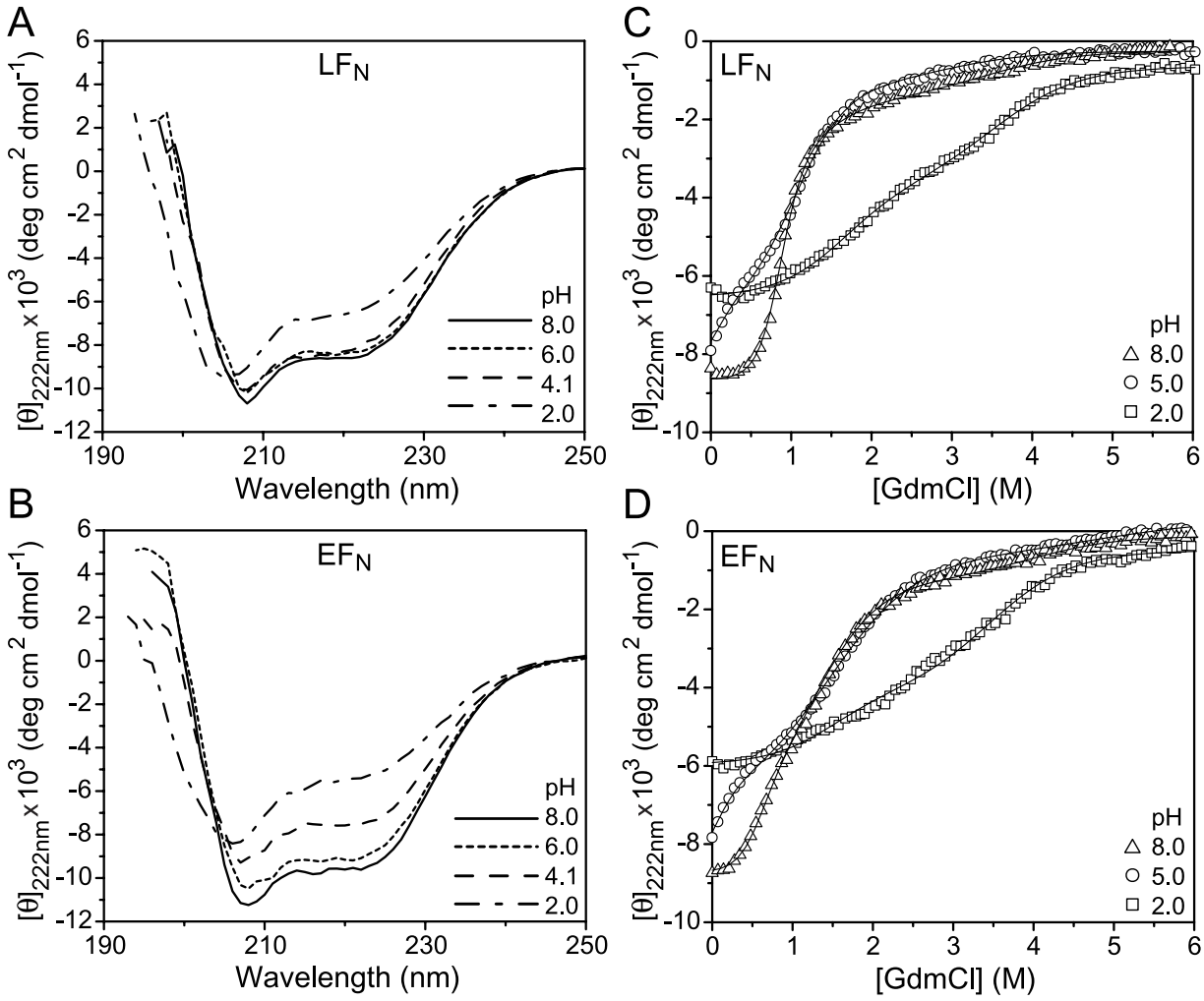

Figure 4. CD spectra and denaturation profiles. Representative CD spectra for (A) LF_N and (B) EF_N each at pH 8.0 (continuous line), 6.0 (dotted line), 4.1 (broken line), and 2.0 (dash-dot line). CD denaturation profiles at 20 °C for (C) LF_N and (D) EF_N at pH 8 (triangles), 5 (circles), and 2 (squares). Profiles are fit to a four-state model. Fit parameters are plotted in Figure 6.

significant solvent penetration dominate I. These complex photophysics, however, preclude unambiguous assignment of N and I signal baselines and further thermodynamic analysis.

4,4′-Dianilino-1,1′-binaphthyl-5,5′-disulfonic acid (bis-ANS) fluorescence

We further characterized the N→I transition using bis-ANS fluorescence to determine if I is a molten globule.[40] Bis-ANS is essentially non-fluorescent until it is bound to apolar sites on a protein; native proteins often do not bind the fluorophore. For LF_N and EF_N, pH titrations reveal an increase in bis-ANS fluorescence that begins at ~pH 7 and plateaus at ~pH 4.5 (Figure 5B). The acid-stabilized I state, therefore, has more apolar bis-ANS-binding sites exposed than the native state. While bis-ANS has considerable hydrophobic surface, it also has two negatively charged sulfonate groups. Thus, some of the additional bis-ANS binding in the acidic pH range may be due to the protonation of Asp/Glu carboxylate groups, which reduces electrostatic repulsion. Nonetheless, the intensity increase is consistent qualitatively with the exposure of significant hydrophobic surface in an MG-like I state.

Fluorescence anisotropy H^+ titrations

We explored several options for characterizing the N→I transition by H^+ titration in the absence of denaturant. Some probes have complex pH-dependent photophysics (Tyr, AF488) or binding properties that artificially drive the thermodynamic transition (bis-ANS). Far-UV CD lacks reasonable signal changes for the two proteins; and near-UV CD is promising, but requires greater concentrations of protein (data not shown). Fluorescence anisotropy, however, is advantageous to the study of pH-dependent protein conformational changes, because it is generally insensitive to pH-dependent changes in fluorophore quantum yield, as the signal is ratiometric. Fluorescence anisotropy senses differences in fluorophore mobility that are expected

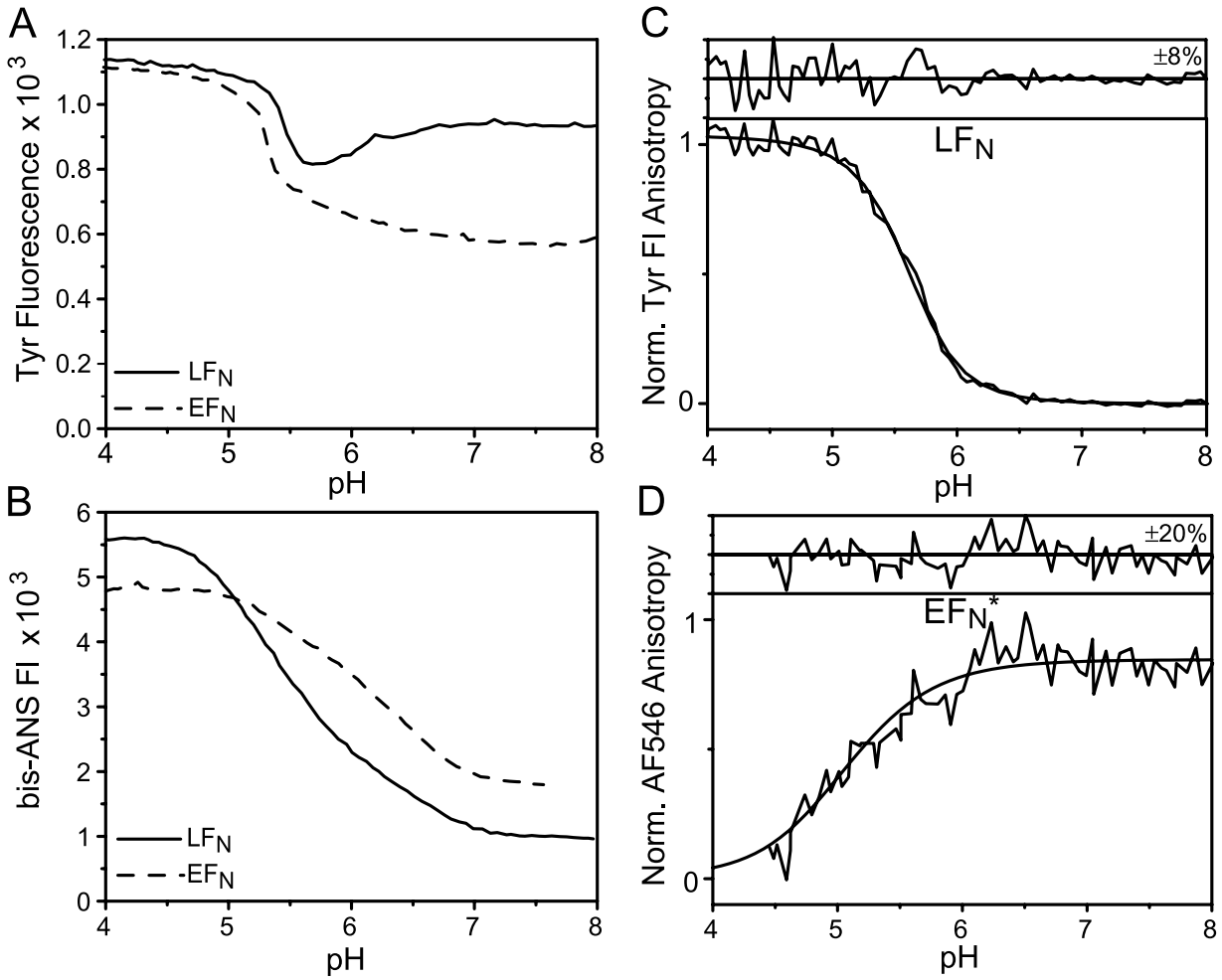

Figure 5. pH titrations in the absence of denaturant. The pH-dependence at 20 °C of (A) Tyr Fl for LF_N (continuous line) and EF_N (broken line), (B) bis-ANS binding fluorescence for LF_N (continuous line) and EF_N (broken line), (C) Tyr Fl anisotropy for LF_N, and (D) AF546 Fl anisotropy for EF_N^*. C and D are fit to equation (3) (Table 2).

when fluorophores change environments as different conformational states are populated. We monitored Tyr Fl anisotropy in the absence of denaturant as a function of pH. LF_N showed a slight, but significant, increase in anisotropy (Figure 5C). The titration curve was fit initially to a single N→I transition (equation (3)), since I was more stable than J, and J was more stable than U. In theory, J should be populated maximally at ~5% near ~pH 5.5 (see Figure 8B), but the data were not of sufficient quality to include the minor population. The pH profile also agrees with separately measured ΔG_{NI} values determined from GdmCl profiles; therefore, pH titration profiles were fit globally with all the available thermodynamic data (Figure 6A). EF_N, however, had such a small Tyr anisotropy signal change that thermodynamic analysis was not feasible (data not shown). H^+ titrations probed by fluorescence anisotropy of directly excited acceptor fluorophores, AF546, in LF_N^* and EF_N^* were performed. From pH 8 to 4, LF_N^* shows an increase in AF546 Fl anisotropy (data not shown), whereas EF_N^*'s anisotropy decreases from 0.17 to 0.15 (Figure 5D).

ΔG pH dependencies

Inspection of the global pH-dependence of the Gibbs free energy changes (Figure 6) shows that a minimum of two classes of titratable/ionizable groups are required to describe the stability changes: one for the destabilization of ΔG_{NI}, ΔG_{IJ} and ΔG_{JU} from pH 7 to 5 and a second for the stabilization of ΔG_{IJ} and ΔG_{JU} from pH 5 to 3. In quantifying the conformational stability changes, we implemented a linked equilibrium binding model[41–43] that relies on the unifying formalism pointed out recently by Hilser and colleagues.[44] This linked equilibrium model demonstrates that presumed pH-dependent changes in *m*-values are indicative of the population of an intermediate. Therefore, we fit all denaturation profiles for the three different optical probes using a shared set of *m*-values, which are invariant with pH (Table 1), and obtained ΔG for each transition as a function of pH. ΔG *versus* pH (Figure 6) was then analyzed by a linked equilibrium proton-binding model (equation (3)) with two classes of ionizable residues: class 1, His; and class 2, Asp/Glu (subscripted 1 and 2

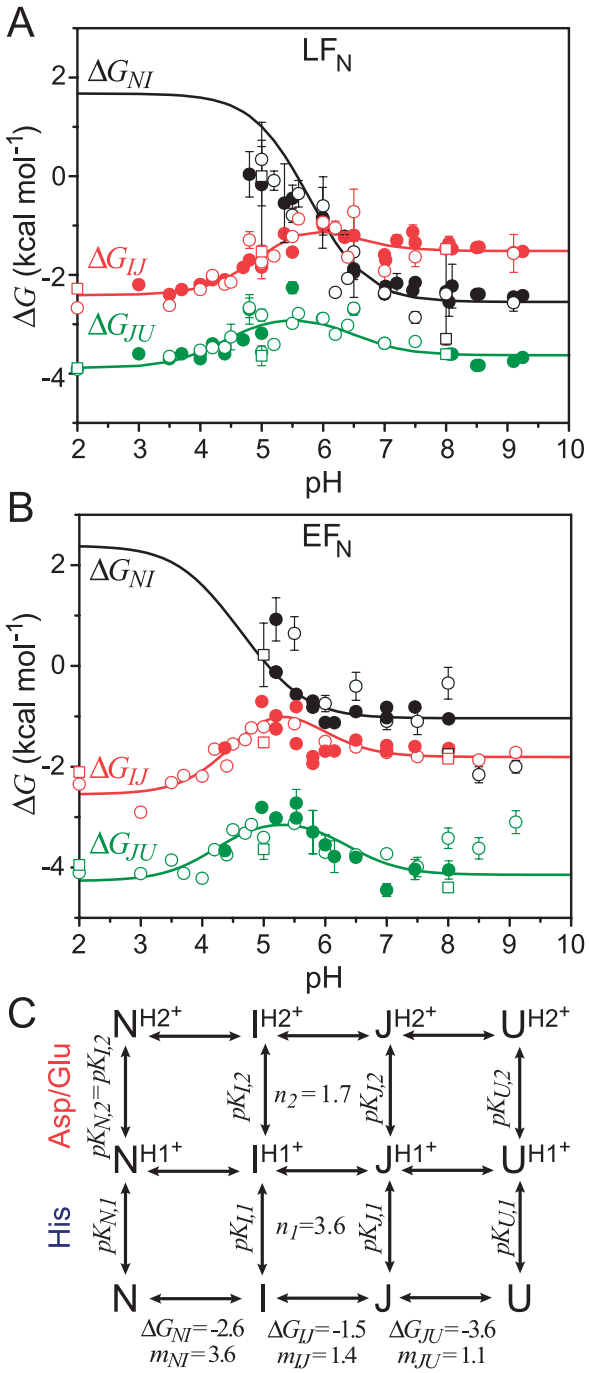

Figure 6. Gibbs free energy pH dependencies. A, LF_N and B, EF_N free energy pH-dependence at 20 °C for each transition, ΔG_{NI} (black symbols), ΔG_{IJ} (red), ΔG_{JU} (green), determined from fits to native Tyr Fl (open circles), FRET (filled circles), and $CD_{222\ nm}$ (open squares). To compensate for missing ΔG_{NI} stability information below pH 5, Fl anisotropy H^+ titrations carried out in the absence of denaturant (Figure 5C and D) were fit simultaneously with the data in A and B using equation (3) (R^2 of 0.996 and 0.993 for LF_N and EF_N, respectively.) C, Four-state linked thermodynamic scheme with two tiers of protonation states, $H1^+$ and $H2^+$; thermodynamic values are given for LF_N.

throughout). It was difficult to estimate ΔG_{NI} below pH 5, so we included fluorescence anisotropy H^+ titrations (Figure 5C and D) in the ΔG *versus* pH fit minimization. As a result, we were able to determine pK values and the number of stability-altering ionizable groups, n (Table 2).

Class 1, histidine

The number of class 1 titratable groups, which affect stability, are ~4 and 2 for LF_N and EF_N, respectively, with pK values that range from 6.6 to 4 (Table 2). For LF_N, we find that $pK_{U,1}$ was near the expected intrinsic value of histidine,[45] where $pK_{I,1}$, $pK_{I,1}$, and $pK_{N,1}$ are successively more depressed. As pK shifts equate to a change in equilibrium stability ($\Delta\Delta G^{H1+}$), LF_N's pattern of successively depressed pK values manifests in a strong destabilization of ΔG_{NI} (~4 kcal mol^{-1}) and milder destabilizations of ΔG_{IJ} and ΔG_{JU} (~1 kcal mol^{-1} in either case; Table 3) by mass action.[43,46,47] This observed acid-denaturation behavior and the range of measured pK values suggest that these residues are desolvated histidine residues. Similar depressed pK values for desolvated His residues, which destabilized the native state, have been observed in apomyoglobin[48–51] and staphylococcal nuclease.[44,52–54] In apomyoglobin, the observed acid-induced transition from N→I is driven by a couple of His residues with very depressed pK values,[51] which may be considered "hot spots".[47,51,55] The alternative view that the loss of globally dispersed charge–charge interactions is responsible for the acid-denaturation is less likely, since such interactions are generally weaker.[55–57]

Under a hot spot hypothesis, analysis of largely desolvated His residues in LF[17] and EF[58] (where those in EF_N are determined by sequence alignment) reveals ten and five residues, respectively, that are >90% desolvated. H91 of LF (96% desolvated) is conserved in EF and may aid in unfolding the amino-terminal domain. Two 100% desolvated His residues in LF, H686 and H690, are responsible for catalytic function,[59] suggesting their dual role: acid-induced denaturation for efficient translocation coupled to catalytic function. Interestingly, LF's H229 is crucial to its binding interaction with PA[15] and is 91% desolvated, implying a dual role as well.

Class 2, aspartate/glutamate

There are two and four class 2 stability-altering groups in LF_N and EF_N, respectively, with pK values that range from 4.1 to 5.4 (Table 2). For LF_N, we find $pK_{U,2}$ is 4.15±0.06 and very near the intrinsic values for Asp or Glu,[45] and $pK_{J,2}$ and $pK_{I,2}$ are successively more elevated. Therefore, the protonation of these acidic residues is stabilizing, leading to increased population of I and J. The reduction of net negative charge may stabilize these condensed, intermediate states, since these proteins have low isoelectric points due to their high content of acidic

Table 2. Proton affinity and stoichiometry

Protein	State	His class[a]		Asp/Glu class[a]		Constraints[b]	R^2
		pK_1	n_1	pK_2	n_2		
LF_N	N	5.34±0.08	3.6±0.4	5.44	1.7±0.1	p$K_{N,2}$=p$K_{I,2}$	0.996
	I	6.21±0.04		5.44±0.05			
	J	6.39±0.05		4.65±0.03			
	U	6.57±0.06		4.15±0.06			
LF_N	N	5.45±0.02	3.72±0.06	5.42[b]	1.67±0.03	p$K_{U,1}$=6.6	0.997
	I	6.24±0.01		5.42±0.03		p$K_{N,2}$=p$K_{I,2}$	
	J	6.41±0.01		4.63±0.01		p$K_{U,2}$=4.1	
	U	6.6[b]		4.1[b]			
EF_N	N	3.9±1	1.74±0.05	4.83[b]	3.8±0.2	p$K_{U,1}$=6.6	0.993
	I	5.37±0.07		4.83±0.05		p$K_{N,2}$=p$K_{I,2}$	
	J	6.09±0.02		4.36±0.01		p$K_{U,2}$=4.1	
	U	6.6[b]		4.1[b]			

Parameters are from fits (equation (3)) to the pH-dependence of ΔG for each transition (Figure 6); goodness of fits are reported by R^2.
[a] Subscripts of pK and n parameters are 1 and 2 for His and Asp/Glu classes, respectively.
[b] Fit model constraints for pK_U are based on those obtained from model compounds.[45]

residues. Interestingly, when these class 2 sites are fully protonated, ΔG_{IU} is more stabilized (−2.9 to −3.7 kcal mol^{-1}) than ΔG_{JU} (−1.1 to −1.3 kcal mol^{-1}; Table 3), demonstrating that the more condensed I state receives more stabilization than the expanded J. The trend may reflect the fact that repulsive electrostatic interactions have shortened length scales that affect compact intermediates more significantly than extended conformers. Compaction also implies increased desolvation in I, which favors elevated pK values, since burial of ionizable groups in the uncharged form is less costly. Because ~50 Asp or Glu residues dominate the surface electrostatics of LF_N and EF_N, acidic residues may contribute as a general collective force, attracting H^+ to the protein through coulombic interactions, elevating their own pK values. As we observed, more compact intermediates express this pK elevation more readily than less compact intermediates.

Desolvation and relative p*K* shifts

The aforementioned solvation effects implicated in the observed pK shifts led us to determine whether these shifts correlate generally with relative surface area burial assessed from m-values. We compute ϕ_{eq}^{H+} as the fraction of the free energy change in the transition between two arbitrary states, i→j, relative to the total change by:

$$\phi_{eq}^{H+}(i \rightarrow j) = \Delta\Delta G_{ij}^{H+}/\Delta\Delta G_{NU}^{H+}$$

where (Table 3):

$$\Delta\Delta G_{ij}^{H+} = 2.30\, nRT(pK_j - pK_i)$$

Table 3. Proton binding stability changes, ϕ-values, and relative surface area burial

Protein	Transition	$\Delta\Delta G^{H1+a}$ (kcal mol^{-1})	$\Delta\Delta G^{H2+a}$ (kcal mol^{-1})	ϕ_{eq}^{H1+b}	ϕ_{eq}^{H2+b}	β_{eq}[c]
LF_N	N→I	4.2±0.6	0[d]	0.71±0.09	0[d]	0.60±0.01
		(3.9±0.1)		(0.69±0.02)		
	I→J	0.9±0.3	−1.8±0.2	0.15±0.05	0.61±0.06	0.23±0.01
		(0.85±0.06)	(−1.77±0.08)	(0.15±0.01)	(0.60±0.03)	[0.58±0.01][c]
	J→U	0.9±0.3	−1.1±0.2	0.15±0.06	0.39±0.06	0.17±0.01
		(0.95±0.03)	(−1.19±0.03)	(0.17±0.01)	(0.40±0.01)	[0.43±0.01][c]
	N→U	6.0±0.8	−2.9±0.3	1[e]	1[e]	1[e]
		(5.7±0.1)	(−2.95±0.09)			
EF_N	N→I	3±2	0[d]	0.5±0.4	0[d]	0.58±0.02
	I→J	1.7±0.2	−2.4±0.3	0.3±0.1	0.64±0.08	0.23±0.01
						[0.55±0.01][c]
	J→U	1.19±0.06	−1.34±0.08	0.20±0.07	0.36±0.03	0.19±0.01
						[0.45±0.01][c]
	N→U	6±2	−3.8±0.3	1[e]	1[e]	1[e]

[a] $\Delta\Delta G$ values for an i→j transition are calculated by $\Delta\Delta G_{ij}^{H+} = 2.30\, nRT(pK_j - pK_i)$ using values in Table 2. Parentheses designate calculations from fit parameters using fixed pK_U values.
[b] Fraction of the total equilibrium free energy change due to protonation in a given transition, i→j, is calculated by $\phi_{eq}^{H+}(i \rightarrow j) = \Delta\Delta G_{ij}^{H+}/\Delta\Delta G_{NU}^{H+}$.
[c] Relative surface area burial, β_{eq}, is defined as m_{ij}/m_{NU} for an i→j transition. Values in square brackets are for the correlation analysis of class 2 residues in Figure 7: due to the inability to assess p$K_{N,2}$, m_{IU} is used instead of m_{NU}.
[d] Zero by definition.
[e] Unity by definition.

For a metric of relative surface burial, we use β_{eq}, which is calculated analogously from *m*-values by $\beta_{eq} = m_{ij}/m_{NU}$ (Table 3). For class 2 residues, we are unable to assess $pK_{N,2}$ and used m_{IU} instead of m_{NU} in the calculation of β_{eq}. A significant correlation between ϕ_{eq}^{H+} and β_{eq} is observed with slope near unity, 1.02 ± 0.05 (*R*-value of 0.936; Figure 7). It may be argued that the correlation reflects the fact that titratable residues with altered p*K* values are distributed over the surface of the protein; however, when specific hydrophobic core residues are mutated, the correlation is recapitulated (unpublished observations). Therefore, p*K* shifts may be due to either (i) global changes in side-chain desolvation and/or (ii) the compaction of charge, which collectively alters the electrostatic field protons encounter when binding the protein. Only the former can apply to class 1 His residues, which have depressed p*K* values, whereas a combination of the former and latter may apply to the class 2 acids, which have elevated p*K* values. Interestingly, desolvation is directly and compaction is indirectly expressed in β_{eq}, contributing to the high degree of correlation.

Discussion

Four-state equilibrium unfolding mechanism

Denaturants are commonly employed in the analysis of a protein's unfolding mechanism, because they allow species that are undetectable under native conditions to be quantified.[33,43,60] The denaturant-dependence of the change in stability is extremely linear, allowing for the facile determination of the free energies of individual transitions. Using optical spectroscopy methods,[33] we have identified a four-state mechanism, N↔I↔J↔U, through the observation of three inflection points in denaturant titrations. Less sophisticated two-state or three-state models led to significant systematic deviations in fit residuals. Denaturant *m*-values, the linear proportionality constant for a given transition's free energy and denaturant concentration, are related empirically[34,60,61] to the solvent-accessible surface area difference between compared states (ΔASA). Therefore, we validate this thermodynamic model by comparing the measured *m*-values to the *ASA* burial change predicted by the structure in the N→U transition.[34] Rigorous assessment of *m*-values allows for detection of intermediates that may be masked when intermediates have signal levels similar to that of the native or unfolded states.[62] Supporting this view, we find that two-state or three-state models underestimate the expected m_{NU}-value significantly, by fourfold and by 2.5-fold, respectively.

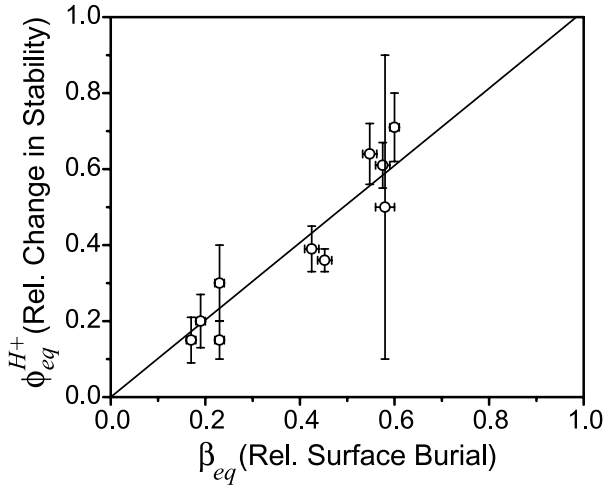

Figure 7. p*K* shifts and desolvation. Correlation of relative surface area buried, β_{eq}, and relative change in equilibrium stability due to protonation, ϕ_{eq}^{H+}, for the three transitions in LF_N and EF_N at class 1 and 2 sites (Table 3), which is fit through the origin (slope of 1.02 ± 0.05; *R*-value of 0.936).

Molten globules and multi-state equilibrium unfolding

Bovine α-lactalbumin and sperm whale myoglobin[63,64] are classic examples of proteins with three-state equilibrium unfolding mechanisms, N↔I↔U. α-Lactalbumin unfolds *via* an MG intermediate (also referred to as the A-state) that is populated heavily under acidic conditions or in moderate concentrations of denaturant in the absence of Ca^{2+}.[21,65,66] This I state retains significant secondary structure as determined by CD studies,[65] and is nearly as compact as the N state,[67] yet despite the rapid accumulation of secondary structure as unfolded protein folds to the I state as detected by CD stopped-flow,[68] hydrogen exchange (HX) studies show dynamic accessibility to the I state's backbone amide groups.[69] For apomyoglobin, the acid-stabilized MG I state, while more stable than U, is closer in Gibbs free energy to U than N.[70] The acid-stabilized MG I state, however, is complex; that is, while HX protection is observed in helices A, G and H of the I state,[71] site-directed mutants demonstrate more significant destabilization of N than I, revealing that tertiary interactions in I are "loose".[72] Likewise, aromatic near-UV CD signals[65] are not preserved in I, indicating a similar loss of tertiary structure in α-lactalbumin.

Four-state equilibrium unfolding systems, N↔I↔J↔U, include DnaK,[73] fibronectin type III domain,[74] α-subunit of tryptophan synthase,[75,76] bovine carbonic anhydrase,[77] and staphylococcal β-lactamase.[78] Low-temperature studies on the latter two reveal both an MG, compact intermediate (~10%>N) and a second, less compact, partly folded, pre-MG intermediate (~30%>N). Hydrodynamic and small-angle X-ray-scattering studies on I1 and I2 of α-subunit of tryptophan synthase[79] demonstrate that while I1 is compact like a MG, I2 is expanded and nearer to the unfolded state but has residual structure.[75,80]

LF_N and EF_N have acid-induced molten globule I states

The I state is shown to be the predominant form under acidic conditions (~pH 5) encountered in endosomes (i.e. in the absence of denaturant; Figure 8A and B). I retains large amounts of secondary structure as determined by far-UV CD (75–90% of N; Figure 3A and B). Yet the acid-driven transition to I liberates ~60% of the native buried ASA (Figure 8B; Table 3). Moreover, acid-induced ASA exposure is confirmed by bis-ANS binding, revealing that the exposed surface is hydrophobic. Near UV-CD studies reveal a loss of aromatic chirality in I (data not shown). Our unpublished Ala/Gly mutagenesis experiments show consistently that at nearly all sites across the protein ~70% of the $\Delta\Delta G$ for each substitution is realized in N, demonstrating that most tertiary interactions are substantially diminished in I. Amino-to-carboxy-terminal FRET distance (r) measurements estimate that I (~60 Å) is compact and closer in this dimension to N (~55 Å) than U (>110 Å). In summary, I is compact, contains substantial secondary structure but little native-like tertiary structure, and consequently, ~14,000 $Å^2$ of surface is exposed in the acid-induced transition.

J is expanded and largely unfolded

The second intermediate, J, shows much less secondary structure content than I. J is more exposed to solvent, as shown by m-value analysis (β_{eq}, Table 3), and its largely quenched Tyr fluorescence signal. Furthermore, FRET distance measurements demonstrate significant expansion in J (~100 Å) relative to N (~55 Å). Interestingly, J is populated maximally (~5%) in the absence of denaturant between pH 5 and 5.5, the physiological conditions expected in endosomes (Figures 1A and 8B). The implication of the minor population of J to translocation, however, is unclear, although it is expected that the translocation intermediate is a threaded polypeptide in a more extended conformation.

Protein unfolding and translocation

The translocation machinery of anthrax toxin (Figure 1A) is contained in the PA moiety. PA_7, upon heptamerization,[7] can bind up to three molecules of LF and/or EF simultaneously.[8] Endocytosis of PA_7-liganded by LF and EF is followed by the trafficking of vesicles containing these complexes to an acidic compartment in the cell.[10] Endosomal acidification then drives PA_7 to an ion-conductive pore form[11] with a 14-stranded β-barrel that spans the membrane.[27,28] LF and EF presumably cross *via* the lumen of the β-barrel, but the lumen is narrow,[11,81] ~15 Å in diameter based on the structure of staphylococcal α-hemolysin[29] (Figure 9A and B).

Our work shows how large, stably folded proteins like LF and EF at neutral pH can be destabilized and partly unfolded under acidic conditions to MG I forms in the absence of ATP-driven chaperones. Regardless of whether the MG I forms of LF_N and EF_N are genuine equilibrium intermediates or more compact denatured states that contain

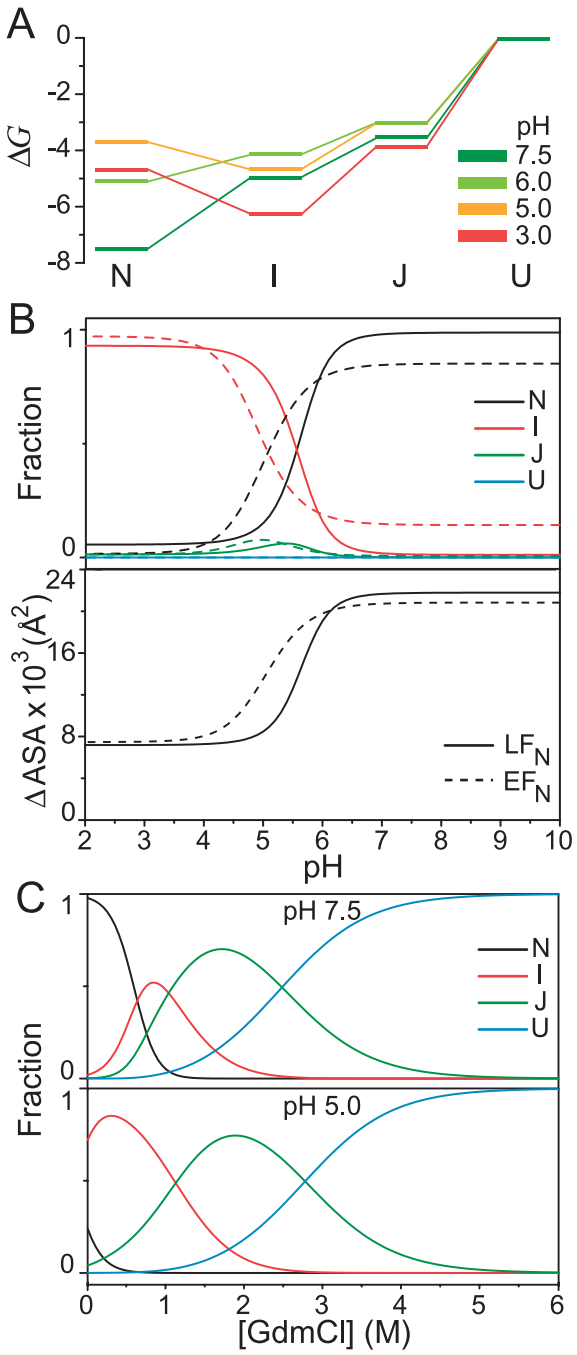

Figure 8. Four-state pH-dependent equilibrium stability model. A, Four-state free energy diagrams for LF_N. B, Simulation of the pH-dependence of the fractional population of the four states (upper panel) and the overall degree of surface area buried relative to U[34] (lower panel) for LF_N (continuous line) and EF_N (broken line). C, Simulations of the GdmCl-dependence of the fractional population of the four states at pH 7.5 (upper panel) and pH 5 (lower) for LF_N.

significant "residual structure", these structures, comprised of ~8000 Å^2 of buried surface and about −8000 deg cm^2 dmole^{-1} ($CD_{222\ nm}$) of secondary structure content, must be either disassembled prior to or accommodated during toxin translocation. The translocation problem, therefore, should consider two key questions. (i) What is the balance of energetic factors that must be overcome upon the conversion of LF_N from a soluble molten form to the "translocating form" that is passable *via* PA pore's lumen? (ii) What are the steric or geometric constraints of polypeptide translocation through a lumen? Namely, which types of likely regular backbone polypeptide conformations can pass through the lumen?

Native state destabilization and dissociation from PA

Once in endosomes, the initial and likely limiting step in the process of anthrax toxin translocation involves the acid-induced destabilization of the native folds of LF and EF. Desolvated His residues (i.e. having p*K* values of ~5 in N) may be, upon protonation, largely responsible. Cell-based translocation studies[14] show that efficient translocation requires pH values below ~5.5 in agreement with the acid-induced N state destabilization observed here (Figures 6A and B, and 8A and B). Recent unpublished data also show that in planar lipid bilayer studies, LF_N translocates *via* the PA_7-pore efficiently (under a +50 mV membrane potential) at pH 5.5 but not pH 6.6, in agreement with our current data.

In conjunction with this acid-induced destabilization, the protein must dissociate from its native state/neutral pH binding site. The largely desolvated H229 in LF and H220 in EF have been shown to be involved in the binding interaction with PA pre-pore heptamer at neutral pH.[15] The acidification of H229 may help LF dissociate from its native/neutral pH binding site. Our unpublished

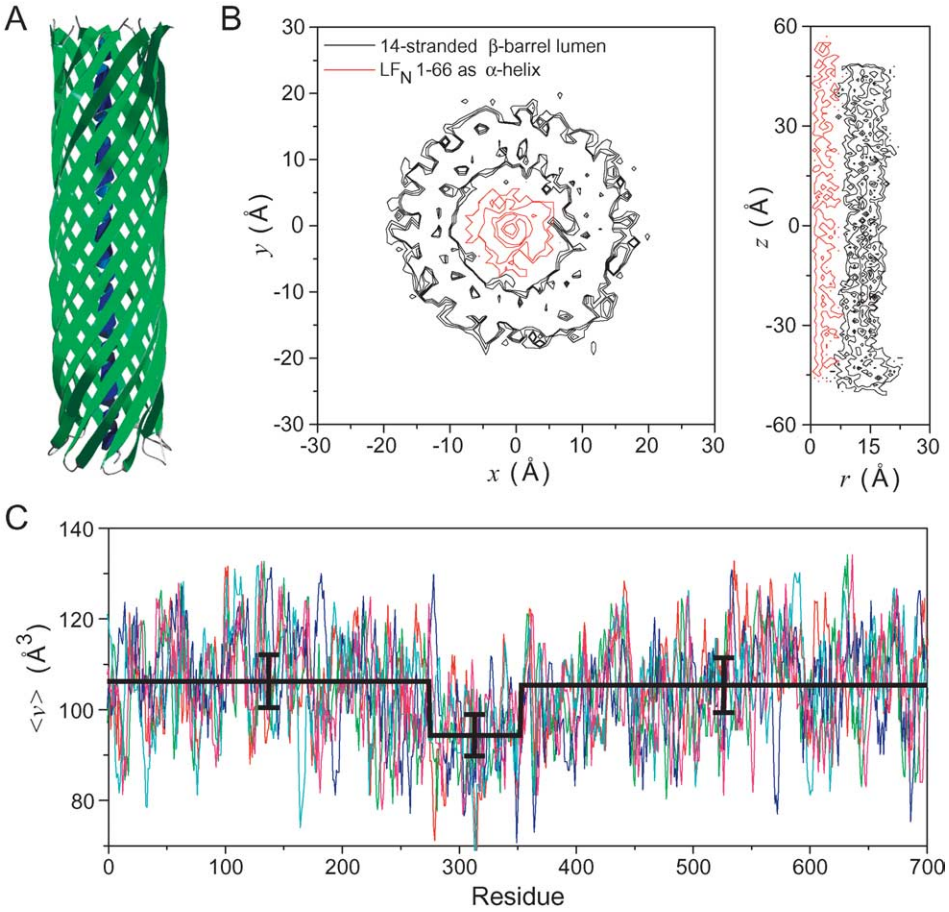

Figure 9. Secondary structure compatibility with PA's β-barrel lumen. A, Model of PA's 14-stranded β-barrel (green) based on staphylococcal α-hemolysin,[29] PA_7s pre-pore structure[13] and other studies,[27,28] where LF_N (residues 1–66 in an α-helical conformation; blue) is in the lumen. Probability contours of the atomic densities, (B) $P(x,y)$ in a bird's eye view (left) and $P(z,r)$ in a radial cross-section view (right), demonstrate little side-chain steric hindrance for a translocating α-helix from LF_N (red contours) in the 14-stranded β-barrel's lumen (black contours). Outermost contours are 1 atom/Å^2. C, Average residue volume, $\langle v \rangle$, calculation on PA and homologues (PA homologue from *Bacillus cereus* G9241 (red), Iota toxin from *Clostridium perfringens* (green), Vip1AC from *B. thuringiensis* (blue), PA from *B. anthracis* (cyan), and Sb component from *C. spiroforme* (magenta)), using a running window of six residues. Three bins of $\langle v \rangle$ for PA and all homologues (thick black line) were made using sequence ranges 1–274, 275–352, and 353–700, where the central bin is the identified luminal β-strands of PA;[28] bin averages are 106(±6) Å^3, 94(±5) Å^3, and 105(±6) Å^3, respectively.

fluorescence data indicate that LF_N changes conformation, dissociating from the native/neutral pH binding site in a pH-dependent manner, in agreement with these acid-denaturation studies. Of course, the binding of LF_N to PA is in linked equilibrium with LF_N's conformational stability; therefore, acid-induced destabilization of LF_N ultimately weakens its apparent affinity for PA at the native/neutral pH binding site.

Conversion of molten globule to a translocatable conformation

Remaining challenges for understanding translocation involve the MG intermediate's residual structure, i.e. retention of native-like secondary structure as well as ~30% of its native buried surface. The energetics under acidic endosomal conditions (~pH 5) are favorable, however, since this MG form is at its minimal stability, only ~1.5 kcal mol^{-1} more stable than the expanded J state (Figure 6A and B), which has only ~3600 $Å^2$ of buried surface and -2500 deg cm^2 $dmol^{-1}$ of $CD_{222\ nm}$. Also, unpublished observations show that tertiary interactions in the MG are loose, i.e. <30% of $\Delta\Delta G_{NU}$. Thus, under acidic conditions the more compact I state is weakly stabilized over the more unfolded J form: favorable energetic interactions gained upon binding inside of PA's lumen may balance the slight penalty paid in melting residual structure in the MG.

Because negatively charged residues are more prevalent than positively charged residues on the surfaces of LF_N and EF_N, and the pore form of PA is cation selective,[11] another critical factor in the conversion of the MG form to a translocatable form is the reduction of net negative charge. Here, the desolvated environment expected in the narrow lumen of PA pore (see Figure 9) probably aids in elevating these acidic residues' p*K* values. This effect is noted in the correlation of ϕ_{eq}^{H+} and β_{eq} in Figure 7, where the relative elevation of p*K* values for class 2 acidic residues, ϕ_{eq}^{H+}, correlates well with desolvation, or β_{eq} computed from *m*-values.

Geometric constraints on translocation

The high content of secondary structure of the MG I forms led us to investigate the geometric constraints imparted by PA_7-pore's β-barrel structure. This 14-stranded β-barrel transmembrane molecular tube structure has been suggested recently by its pre-pore structure[13] and the alternating pattern of accessibility to sulfhydryl-modification in cysteine-substituted mutants of PA assessed by K^+ conductance measurements, using black membranes.[27,28] Tetraalkylammonium ion studies indicated that the lumen is at least ~11 Å in diameter.[81] The structure of PA's β-barrel lumen is believed to be similar to staphylococcal α-hemolysin[29] due to their similar 7-fold symmetries and the number of hydrophobic residues spanning the membrane.[27] There may, however, be subtle differences in the angular alignment or shear, *S*, in PA's luminal β-strands.[82] A recent structure of an autotransporter, NalP, has revealed a 12-stranded transmembrane β-barrel, in which the lumen of the translocator domain is filled with an α-helical tail of the passenger domain.[83] Likewise, this model of PA's β-barrel lumen (Figure 9A) shows that α-helix may be accommodated, making residual secondary structure in the MG form of LF and EF less of a factor than anticipated (Figure 9B). Other backbone conformers, such as extended β-strand or polyproline II, a common element of unfolded polypeptides,[84–86] are considerably more narrow than α-helix. Therefore, the translocator domain of a 14-stranded β-barrel tube can pass, in principle, all elements of secondary structure but probably not tertiary structure. Analysis of average residue volume, $\langle v \rangle$, shows selection pressure in PA and related pore-forming toxins for smaller side-chains in the luminal β-strands (Figure 9C). We conclude that the cross-sectional area of the lumen is optimized for the passage of even the bulkiest secondary structural elements, such as α-helix.

We also observed the conservation of small volume residues with alcohol functional groups, Ser and Thr, in the lumen's interior. A prior study of the inventories of side-chains in related β-barrel outer membrane proteins in Gram-negative bacteria[87] showed general conservation of Ser and Thr in the interior, luminal face, but did not conclude on their chemical or steric utility in the translocation of polypeptides. The simplest explanation may be that these residues best mimic water and have favorable solvation characteristics for translocating peptides or substrates. Co-solvent alcohols, especially 2,2,2-trifluoroethanol,[88] promote α-helical conformations in proteins and unstructured peptides, probably by favoring backbone desolvation.[89,90] Also, α-helix formation has been shown to be coupled with surface area burial in protein folding transition states, presumably due to desolvation.[91,92] Furthermore, the narrowness of the lumen (Figure 9B) limits the amount of solvent that may be permitted to translocate alongside the polypeptide, enhancing the aforementioned helix-stabilizing effects.

The snug fit of the α-helix in the structure of NalP led Oomen *et al.* to consider that helix is not the major secondary structural element populated during translocation, and an accessory chaperone, Omp85, may assist the translocation of the passenger domain. However, we conclude that the lumen can accommodate α-helix, and the steric constraints and chemical composition of the lumen's interior may promote α-helix formation.

Conclusion

We have demonstrated that LF and EF's amino-terminal domains unfold *via* two intermediate

states, I and J. State I is a classic MG that is populated heavily at low pH conditions, consistent with those physiologically relevant to acidified endosomes. The pH-dependence is likely attributable to desolvated His residues in N that have depressed p*K* values. Desolvated histidine residues are distributed throughout the structures of LF and EF. The acid-induced I state contains substantial secondary structure. Yet sequence analysis and modeling studies show conservation of small volume residues in PA's β-barrel lumen, which maximize its ability to translocate secondary structures as large as α-helix but not tertiary structures. Acid-denaturation of LF and EF define the initial events of translocation and explain how large proteins may travel through a narrow channel in the absence of ATP-driven chaperones. While we have not studied the full-length ~90 kDa versions of LF and EF (for technical reasons), future work will address whether the observed pH-dependent destabilization of the enzymatic moieties' PA-binding domains are recapitulated in their catalytic domains. Finally, current work demonstrating that membrane potential is a driving force for translocation undoubtedly sets the course for understanding how protein folding is coupled with translocation.

Materials and Methods

Proteins

K14C and N242C mutations were introduced into an over-expression plasmid, pET15b-LF_N (residues 1–263 of LF[15]). Likewise, H4C and G241C were introduced into pET15b-EF_N (residues 1–254 of EF[15]). Proteins were over-expressed in a 5 l fermenter using ECPM1 broth.[93] Extracts were His_6 affinity purified;[15] pure fractions (concentrated to 30 g/l) were treated with 5 mM DTT and stored at −80 °C.

FRET labeling

Buffers A (20 mM Tris–HCl, pH 8) and B (buffer A + 1 M NaCl) were purged of O_2 by sparging with N_2. A portion (~1 μmol) of DTT-free, dual Cys LF_N or EF_N was reacted with 1 mg of Alexa Fluor 488-C_5-maleimide (AF488, Molecular Probes) for two hours at 25 °C in 0.5 mM tris-(2-carboxyethyl)phosphine (TCEP). Unreacted dye was blocked with 10 mM 2-mercaptoethanol. After concentrating to ~2 ml, reactions were separated into four species, free dye, unlabeled protein, singly labeled protein, and doubly labeled protein, using Hi-Trap Q Sepharose anion-exchange, HTQ (0–500 mM NaCl gradient in bufferA; 280 nm/495 nm absorbance detection). Protein peaks were assessed by SDS-PAGE and absorbance. Single AF488-labeled protein was then reacted with 0.5 mg of Alexa Fluor 546-C_5-maleimide (AF546) and HTQ purified. Labeling efficiency was assessed using the manufacturer's ratiometric absorbance procedure.

FI and CD equilibrium denaturation

Generally in denaturant titrations, the cuvette contained buffer with 0 M GdmCl, and the titrant contained 6–7 M GdmCl, where the protein concentration was identical in the two solutions. A computer-controlled Hamilton titrator was interfaced to either a Jasco J-715 spectropolarimeter for CD (222(±2) nm) or an ISS K-2 fluorimeter for Tyr Fl (excitation 275(±16) nm, emission 330(±16) nm) and FRET (excitation 488 nm, emission ratio of 520 to 570(±16) nm). Protein concentrations ranged from 10 nM to 2 μM. Experiments used either fluorescence universal buffer (FUB: 10 mM each Tris–HCl, Mes, Hepes and acetic acid) or CD universal buffer (CDUB: 10 mM each borate, phosphate, and acetic acid). For fluorescence spectra, monochromator slit-widths were reduced to ±8 nm. For CD spectra, degassed 5 mM phosphoric acid adjusted in pH with NaOH was used instead of CDUB.

The unfolding reaction was shown to be reversible by numerous controls: GdmCl, urea, H^+ and temperature-denatured LF_N all refolded to their native folds as indicated by $CD_{222\ nm}$, native Tyr fluorescence and bis-ANS binding fluorescence. The timescales of refolding relaxation from chemically denatured conditions were faster than one second; therefore, 10–20 seconds of equilibration time was allotted per titration step.

Equilibrium fluorescence H^+ titrations

For Tyr fluorescence experiments, cuvettes contained 0.5 μM LF_N or EF_N at pH ~8 in FUB. Titrant solutions, which contained 0.5 μM protein, in FUB (~pH 2–3), were added in 20–40 μl increments by the Hamilton titrator to the cuvette, spanning pH 8–4. The pH was monitored continuously by a 3.5 mm Orion micro probe (type 8102) interfaced to a Jenco 6171 console that outputs a voltage signal proportional to pH, which was recorded by the fluorimeter's analog input for a photomultiplier tube. Bis-ANS binding fluorescence intensity experiments (excitation 340(±16) nm, emission >500 nm filter) used FUB supplemented with 10 μM bis-ANS at protein concentrations of 100 nM.

Anisotropy fluorescence

Tyr fluorescence and AF546 fluorescence anisotropy were measured in FUB, where the former was excited at 275(±16) nm by a vertically polarized xenon arc lamp and the latter was excited by a 514 nm Ar^+ laser line. A Glan-Thompson polarizing prism was stepped in orthogonal intervals per titration point to record vertically (F_{vert}) and horizontally (F_{hor}) polarized intensities at 330(±16) nm for Tyr and 570(±16) nm for AF546. Anisotropy, *a*, is calculated by:

$$a = \frac{F_{vert} - F_{hor}}{F_{vert} + 2F_{hor}}$$

Protein concentrations were 2 μM and 150 nM for Tyr and AF546 anisotropy measurements, respectively.

Four-state thermodynamic model

For a N↔I↔J↔U equilibrium model containing native (N), unfolded (U) and two intermediate states (I and J), the partition function, *Q*, which describes the total energy of the system, is:

$$Q = 1 + K_{NI} + K_{NI}K_{IJ} + K_{NI}K_{IJ}K_{JU} \quad (1)$$

Fractional populations, f, of each state are:

$$f_N = \frac{1}{Q},\quad f_I = \frac{K_{NI}}{Q},\quad f_J = \frac{K_{NI}K_{IJ}}{Q} \text{ and } f_U = \frac{K_{NI}K_{IJ}K_{JU}}{Q} \tag{2}$$

Denaturant and pH-dependence for the equilibrium constants, K, between any two states, i and j, of this set, {N, I, J,U}, are:

$$K_{ij}([\text{Den}], \text{p}H) = K_{ij}\exp(m_{ij}[\text{Den}]/RT)\prod_k \left(\frac{1+10^{\text{p}K_{i,k}-\text{p}H}}{1+10^{\text{p}K_{j,k}-\text{p}H}}\right)^{n_k} \tag{3}$$

Free energy changes between any states i and j (in the absence of denaturant at $\text{pH} \gg \text{p}K$) are given by $\Delta G = RT \ln K_{ij}$. ΔG values for a given transition have a linear free energy destabilization with respect to [Den] with a proportionality of m.[32,33] The pH-dependence is defined using Wyman's linkage, in which n protons bind to n ionizable groups in state i and j with affinities described by $\text{p}K_i$ and $\text{p}K_j$, respectively; $\text{p}K = -\log K_a$, and K_a is a proton dissociation equilibrium constant.[41–43] Two classes of ionizable groups are indexed by k in the set, {His, Asp/Glu}. Observed signals, θ_{obs}, for a denaturant or pH titration are given as $\theta_{obs} = \sum_i f_i\theta_i$.

Four-state denaturation profile analysis

Assuming m-values were invariant with pH,[44] profiles were fit initially in clusters (e.g. high, pH 6.5–9.5; medium, pH 5–6.5; and low, pH 2–5), where the m-values were defined as globally shared parameters in each cluster. The m-value describing the N→I transition was determined only from the high pH datasets. Thus, for the medium set, m_{NI} was fixed and m_{IJ} and m_{JU} were obtained. For the low set of data, the profiles were essentially fit to a three-state model, I↔J↔U, because ΔG_{NI} was too destabilized to measure. After a consistent set of m-values were estimated, all denaturation profiles were fit by equation (3) to obtain ΔG values. Only a sloping baseline correction was made for Tyr fluorescence, since GdmCl had a fluorescent background. Finally, ΔG *versus* pH was fit to equation (3). Fluorescence anisotropy pH titrations were included in the global, non-linear, least-squares fit of the ΔG values to best estimate $\text{p}K_{N,1}$ under acidic destabilizing conditions. Constraints, in some cases, were applied for LF_N and EF_N as defined in Table 2 for the intrinsic pK values of His and Asp/Glu, in U.

FRET distance measurements

A steady state protocol[30] estimated the FRET efficiency of N, E_N. By the Förster relationship, FRET distance, r, for an efficiency, E, of any state i is $r_i = \sqrt[6]{R_o^6(1/E_i - 1)}$, where the Förster distance, R_o, for AF488 and AF546 is 60 Å (Molecular Probes). E for an intermediate species i was approximated using the signal intensities, θ_I and θ_J, from equilibrium denaturation fits and the FRET distance in N, r_N, by:

$$E_i = (R_o^6/(R_o^6 + r_N^6)) \times \left(\theta_i/(\theta_N - \theta_U)\right)$$

Surface area and structure modeling

GETAREA 1.1† calculated ASA with a solvent radius of 1.4 Å.[94] Coordinates of LF_N (residues 27–263; 1J7N)[17] were modified to include a disordered N terminus using Swiss-PdbViewer.[95] A U model of LF_N was created by extending ϕ/ψ angles to 180°.[34] An α-helical model ($\phi = -57°$, $\psi = -47°$) of residues 1–66 of LF_N was made using Swiss-PdbViewer. A model of PA's β-barrel transmembrane lumen was generated by populating 7AHL[29] with side-chains from PA defined as "inside" and "outside" of the lumen from a previous study.[28] The β-barrel of PA and α-helical model of LF_N were aligned along their symmetry axes to the z-axis to calculate probability contour histograms (1×1 Å bins): (i) $P(x,y)$, for a bird's eye view; and (ii) $P(r,z)$, for a cross-sectional view of atomic density at radius, r, from the z-axis.

A running window calculation of average side-chain volume, $\langle v \rangle_i$, was made from individual residue volumes, v,[96] where $\langle v \rangle_i = \sum_{j=i}^{i+l-1} \frac{v_j}{l}$ for a window length, $l = 6$ residues, using the following sequences: PA homolog from *B. cereus* G9241 (accession no. ZP_00236306), Iota toxin from *C. perfringens* (I40862), Vip1AC from *B. thuringiensis* (AAO86514), PA from *B. anthracis* (I39934), and Sb component from *C. spiroforme* (CAA66612), where the ~30 residue secretion tag leaders were removed.

Acknowledgements

We thank members of the laboratory, especially R. A. Melnyk and D. B. Lacy for discussions of β-barrel proteins. We thank D. B. Lacy, T. R. Sosnick, and A. Finkelstein for their critical reading of the manuscript. This work was supported by an NRSA fellowship, AI062204-01 (to B. A. K.), and NIH grant, AI022021-21 (to R. J. C.).

References

1. Duesbery, N. S., Webb, C. P., Leppla, S. H., Gordon, V. M., Klimpel, K. R., Copeland, T. D. *et al*. (1998). Proteolytic inactivation of MAP-kinase-kinase by anthrax lethal factor. *Science*, **280**, 734–737.
2. Vitale, G., Pellizzari, R., Recchi, C., Napolitani, G., Mock, M. & Montecucco, C. (1998). Anthrax lethal factor cleaves the N-terminus of MAPKKs and induces tyrosine/threonine phosphorylation of MAPKs in cultured macrophages. *Biochem. Biophys. Res. Commun.* **248**, 706–711.
3. Leppla, S. H. (1982). Anthrax toxin edema factor: a bacterial adenylate cyclase that increases cyclic AMP concentrations of eukaryotic cells. *Proc. Natl Acad. Sci. USA*, **79**, 3162–3166.
4. Bradley, K. A., Mogridge, J., Mourez, M., Collier, R. J. & Young, J. A. (2001). Identification of the cellular receptor for anthrax toxin. *Nature*, **414**, 225–229.
5. Scobie, H. M., Rainey, G. J. A., Bradley, K. A. & Young, J. A. (2003). Human capillary morphogenesis protein 2 functions as an anthrax toxin receptor. *Proc. Natl Acad. Sci. USA*, **100**, 5170–5174.
6. Molloy, S. S., Bresnahan, P. A., Leppla, S. H., Klimpel,

† http://www.scsb.utmb.edu/cgi-bin/get_a_form.tcl

K. R. & Thomas, G. (1992). Human furin is a calcium-dependent serine endoprotease that recognizes the sequence Arg-X-X-Arg and efficiently cleaves anthrax toxin protective antigen. *J. Biol. Chem.* **267**, 16396–16402.
7. Milne, J. C., Furlong, D., Hanna, P. C., Wall, J. S. & Collier, R. J. (1994). Anthrax protective antigen forms oligomers during intoxication of mammalian cells. *J. Biol. Chem.* **269**, 20607–20612.
8. Mogridge, J., Cunningham, K. & Collier, R. J. (2002). Stoichiometry of anthrax toxin complexes. *Biochemistry,* **41**, 1079–1082.
9. Elliott, J. L., Mogridge, J. & Collier, R. J. (2000). A quantitative study of the interactions of *Bacillus anthracis* edema factor and lethal factor with activated protective antigen. *Biochemistry,* **39**, 6706–6713.
10. Friedlander, A. M. (1986). Macrophages are sensitive to anthrax lethal toxin through an acid-dependent process. *J. Biol. Chem.* **261**, 7123–7126.
11. Blaustein, R. O., Koehler, T. M., Collier, R. J. & Finkelstein, A. (1989). Anthrax toxin: channel-forming activity of protective antigen in planar phospholipid bilayers. *Proc. Natl Acad. Sci. USA*, **86**, 2209–2213.
12. Miller, C. J., Elliott, J. L. & Collier, R. J. (1999). Anthrax protective antigen: prepore-to-pore conversion. *Biochemistry,* **38**, 10432–10441.
13. Petosa, C., Collier, R. J., Klimpel, K. R., Leppla, S. H. & Liddington, R. C. (1997). Crystal structure of the anthrax toxin protective antigen. *Nature*, **385**, 833–838.
14. Wesche, J., Elliott, J. L., Falnes, P. O., Olsnes, S. & Collier, R. J. (1998). Characterization of membrane translocation by anthrax protective antigen. *Biochemistry,* **37**, 15737–15746.
15. Lacy, D. B., Mourez, M., Fouassier, A. & Collier, R. J. (2002). Mapping the anthrax protective antigen binding site on the lethal and edema factors. *J. Biol. Chem.* **277**, 3006–3010.
16. Kelley, L. A., MacCallum, R. M. & Sternberg, M. J. (2000). Enhanced genome annotation using structural profiles in the program 3D-PSSM. *J. Mol. Biol.* **299**, 499–520.
17. Pannifer, A. D., Wong, T. Y., Schwarzenbacher, R., Renatus, M., Petosa, C., Bienkowska, J. *et al*. (2001). Crystal structure of the anthrax lethal factor. *Nature*, **414**, 229–233.
18. Ohgushi, M. & Wada, A. (1983). Molten-globule state: a compact form of globular proteins with mobile side-chains. *FEBS Letters*, **164**, 21–24.
19. Dolgikh, D. A., Gilmanshin, R. I., Brazhnikov, E. V., Bychkova, V. E., Semisotnov, G. V., Venyaminov, S. Y. & Ptitsyn, O. B. (1981). α-lactalbumin; compact state with fluctuating tertiary structure? *FEBS Letters*, **136**, 311–315.
20. Ptitsyn, O. B., Pain, R. H., Semisotnov, G. V., Zerovnik, E. & Razgulyaev, O. I. (1990). Evidence for a molten globule state as a general intermediate in protein folding. *FEBS Letters*, **262**, 20–24.
21. Kuwajima, K. (1989). The molten globule state as a clue for understanding the folding and cooperativity of globular-protein structure. *Proteins: Struct. Funct. Genet.* **6**, 87–103.
22. Bychkova, V. E., Pain, R. H. & Ptitsyn, O. B. (1988). The "molten globule" state is involved in the translocation of proteins across membranes? *FEBS Letters*, **238**, 231–234.
23. van der Goot, F. G., Gonzalez-Manas, J. M., Lakey, J. H. & Pattus, F. (1991). A "molten-globule" membrane-insertion intermediate of the pore-forming domain of colicin A. *Nature*, **354**, 408–410.
24. van der Goot, F. G., Lakey, J. H. & Pattus, F. (1992). The molten globule intermediate for protein insertion or translocation through membranes. *Trends Cell Biol.* **2**, 343–348.
25. Zhao, J. M. & London, E. (1986). Similarity of the conformation of diphtheria toxin at high temperature to that in the membrane-penetrating low-pH state. *Proc. Natl Acad. Sci. USA*, **83**, 2002–2006.
26. Ren, J., Kachel, K., Kim, H., Malenbaum, S. E., Collier, R. J. & London, E. (1999). Interaction of diphtheria toxin T domain with molten globule-like proteins and its implications for translocation. *Science*, **284**, 955–957.
27. Benson, E. L., Huynh, P. D., Finkelstein, A. & Collier, R. J. (1998). Identification of residues lining the anthrax protective antigen channel. *Biochemistry,* **37**, 3941–3948.
28. Nassi, S., Collier, R. J. & Finkelstein, A. (2002). PA63 channel of anthrax toxin: an extended β-barrel. *Biochemistry,* **41**, 1445–1450.
29. Song, L., Hobaugh, M. R., Shustak, C., Cheley, S., Bayley, H. & Gouaux, J. E. (1996). Structure of staphylococcal α-hemolysin, a heptameric transmembrane pore. *Science*, **274**, 1859–1866.
30. Hoppe, A., Christensen, K. & Swanson, J. A. (2002). Fluorescence resonance energy transfer-based stoichiometry in living cells. *Biophys. J.* **83**, 3652–3664.
31. Millett, I. S., Doniach, S. & Plaxco, K. W. (2002). Toward a taxonomy of the denatured state: small angle scattering studies of unfolded proteins. *Advan. Protein Chem.* **62**, 241–262.
32. Greene, R. F., Jr & Pace, C. N. (1974). Urea and guanidine hydrochloride denaturation of ribonuclease, lysozyme, α-chymotrypsin, and β-lactoglobulin. *J. Biol. Chem.* **249**, 5388–5393.
33. Pace, C. N. (1986). Determination and analysis of urea and guanidine hydrochloride denaturation curves. *Methods Enzymol.* **131**, 266–280.
34. Myers, J. K., Pace, C. N. & Scholtz, J. M. (1995). Denaturant *m* values and heat capacity changes: relation to changes in accessible surface areas of protein unfolding. *Protein Sci.* **4**, 2138–2148.
35. Lee, B. & Richards, F. M. (1971). The interpretation of protein structures: estimation of static accessibility. *J. Mol. Biol.* **55**, 379–400.
36. Saxena, V. P. & Wetlaufer, D. B. (1971). A new basis for interpreting the circular dichroic spectra of proteins. *Proc. Natl Acad. Sci. USA*, **68**, 969–972.
37. Willis, K. J. & Szabo, A. G. (1991). Fluorescence decay kinetics of tyrosinate and tyrosine hydrogen-bonded complexes. *J. Phys. Chem.* **95**, 1585–1589.
38. Rayner, D. M., Krajcarski, D. T. & Szabo, A. G. (1978). Excited-state acid–base equilibrium of tyrosine. *Can. J. Chem.* **56**, 1238–1245.
39. Pal, H., Palit, D. K., Mukherjee, T. & Mittal, J. P. (1990). Some aspects of steady state and time-resolved fluorescence of tyrosine and related compounds. *J. Photochem. Photobiol. A*, **52**, 391–409.
40. Shi, L., Palleros, D. R. & Fink, A. L. (1994). Protein conformational changes induced by 1,1′-bis(4-anilino-5-naphthalenesulfonic acid): preferential binding to the molten globule of DnaK. *Biochemistry,* **33**, 7536–7546.
41. Wyman, J., Jr (1964). Linked functions and reciprocal effects in hemoglobin: a second look. *Advan. Protein Chem.* **19**, 223–286.
42. Wyman, J., Jr & Gill, S. (1990). *Binding and Linkage*. University Science Books, Mill Valley, CA.

43. Tanford, C. (1970). Protein denaturation. C. Theoretical models for the mechanism of denaturation. *Advan. Protein Chem.* **24**, 1–95.
44. Whitten, S. T., Wooll, J. O., Razeghifard, R., Garcia-Moreno, E.B & Hilser, V. J. (2001). The origin of pH-dependent changes in *m*-values for the denaturant-induced unfolding of proteins. *J. Mol. Biol.* **309**, 1165–1175.
45. Creighton, T. E., Jr (1993). *Proteins: Structures and Molecular Properties*. W.H. Freeman, New York.
46. Yang, A. S., Gunner, M. R., Sampogna, R., Sharp, K. & Honig, B. (1993). On the calculation of pK_as in proteins. *Proteins: Struct. Funct. Genet.* **15**, 252–265.
47. Yang, A. S. & Honig, B. (1993). On the pH dependence of protein stability. *J. Mol. Biol.* **231**, 459–474.
48. Barrick, D. & Baldwin, R. L. (1993). The molten globule intermediate of apomyoglobin and the process of protein folding. *Protein Sci.* **2**, 869–876.
49. Cocco, M. J., Kao, Y. H., Phillips, A. T. & Lecomte, J. T. (1992). Structural comparison of apomyoglobin and metaquomyoglobin: pH titration of histidines by NMR spectroscopy. *Biochemistry*, **31**, 6481–6491.
50. Cocco, M. J. & Lecomte, J. T. (1994). The native state of apomyoglobin described by proton NMR spectroscopy: interaction with the paramagnetic probe HyTEMPO and the fluorescent dye ANS. *Protein Sci.* **3**, 267–281.
51. Yang, A. S. & Honig, B. (1994). Structural origins of pH and ionic strength effects on protein stability. Acid denaturation of sperm whale apomyoglobin. *J. Mol. Biol.* **237**, 602–614.
52. Ionescu, R. M. & Eftink, M. R. (1997). Global analysis of the acid-induced and urea-induced unfolding of staphylococcal nuclease and two of its variants. *Biochemistry*, **36**, 1129–1140.
53. Alexandrescu, A. T., Mills, D. A., Ulrich, E. L., Chinami, M. & Markley, J. L. (1988). NMR assignments of the four histidines of staphylococcal nuclease in native and denatured states. *Biochemistry*, **27**, 2158–2165.
54. Lee, K. K., Fitch, C. A., Lecomte, J. T. & Garcia-Moreno, E. B. (2002). Electrostatic effects in highly charged proteins: salt sensitivity of pK_a values of histidines in staphylococcal nuclease. *Biochemistry*, **41**, 5656–5667.
55. Honig, B. & Yang, A. S. (1995). Free energy balance in protein folding. *Advan. Protein Chem.* **46**, 27–58.
56. Pace, C. N., Laurents, D. V. & Thomson, J. A. (1990). pH dependence of the urea and guanidine hydrochloride denaturation of ribonuclease A and ribonuclease T1. *Biochemistry*, **29**, 2564–2572.
57. Pace, C. N., Laurents, D. V. & Erickson, R. E. (1992). Urea denaturation of barnase: pH dependence and characterization of the unfolded state. *Biochemistry*, **31**, 2728–2734.
58. Drum, C. L., Yan, S. Z., Bard, J., Shen, Y. Q., Lu, D., Soelaiman, S. *et al*. (2002). Structural basis for the activation of anthrax adenylyl cyclase exotoxin by calmodulin. *Nature*, **415**, 396–402.
59. Klimpel, K. R., Arora, N. & Leppla, S. H. (1994). Anthrax toxin lethal factor contains a zinc metalloprotease consensus sequence which is required for lethal toxin activity. *Mol. Microbiol.* **13**, 1093–1100.
60. Schellman, J. A. (1987). Selective binding and solvent denaturation. *Biopolymers*, **26**, 549–559.
61. Shortle, D. (1995). Staphylococcal nuclease: a showcase of *m*-value effects. *Advan. Protein Chem.* **46**, 217–247.
62. Soulages, J. L. (1998). Chemical denaturation: potential impact of undetected intermediates in the free energy of unfolding and *m*-values obtained from a two-state assumption. *Biophys. J.* **75**, 484–492.
63. Goto, Y. & Fink, A. L. (1990). Phase diagram for acidic conformational states of apomyoglobin. *J. Mol. Biol.* **214**, 803–805.
64. Hughson, F. M., Wright, P. E. & Baldwin, R. L. (1990). Structural characterization of a partly folded apomyoglobin intermediate. *Science*, **249**, 1544–1548.
65. Kuwajima, K., Nitta, K., Yoneyama, M. & Sugai, S. (1976). Three-state denaturation of α-lactalbumin by guanidine hydrochloride. *J. Mol. Biol.* **106**, 359–373.
66. Kuwajima, K. (1996). The molten globule state of α-lactalbumin. *FASEB J.* **10**, 102–109.
67. Kataoka, M., Kuwajima, K., Tokunaga, F. & Goto, Y. (1997). Structural characterization of the molten globule of α-lactalbumin by solution X-ray scattering. *Protein Sci.* **6**, 422–430.
68. Nozaka, M., Kuwajima, K., Nitta, K. & Sugai, S. (1978). Detection and characterization of the intermediate on the folding pathway of human α-lactalbumin. *Biochemistry*, **17**, 3753–3758.
69. Dolgikh, D. A., Abaturov, L. V., Bolotina, I. A., Brazhnikov, E. V., Bychkova, V. E., Gilmanshin, R. L. *et al*. (1985). Compact state of a protein molecule with pronounced small-scale mobility: bovine α-lactalbumin. *Eur. Biophys. J.* **13**, 109–121.
70. Barrick, D. & Baldwin, R. L. (1993). Three-state analysis of sperm whale apomyoglobin folding. *Biochemistry*, **32**, 3790–3796.
71. Jennings, P. A. & Wright, P. E. (1993). Formation of a molten globule intermediate early in the kinetic folding pathway of apomyoglobin. *Science*, **262**, 892–896.
72. Hughson, F. M., Barrick, D. & Baldwin, R. L. (1991). Probing the stability of a partly folded apomyoglobin intermediate by site-directed mutagenesis. *Biochemistry*, **30**, 4113–4118.
73. Montgomery, D., Jordan, R., McMacken, R. & Freire, E. (1993). Thermodynamic and structural analysis of the folding/unfolding transitions of the *Escherichia coli* molecular chaperone DnaK. *J. Mol. Biol.* **232**, 680–692.
74. Patel, S., Chaffotte, A. F., Goubard, F. & Pauthe, E. (2004). Urea-induced sequential unfolding of fibronectin: a fluorescence spectroscopy and circular dichroism study. *Biochemistry*, **43**, 1724–1735.
75. Saab-Rincon, G., Froebe, C. L. & Matthews, C. R. (1993). Urea-induced unfolding of the α subunit of tryptophan synthase: one-dimensional proton NMR evidence for residual structure near histidine-92 at high denaturant concentration. *Biochemistry*, **32**, 13981–13990.
76. Matthews, C. R. & Crisanti, M. M. (1981). Urea-induced unfolding of the α subunit of tryptophan synthase: evidence for a multistate process. *Biochemistry*, **20**, 784–792.
77. Uversky, V. N. & Ptitsyn, O. B. (1996). Further evidence on the equilibrium "pre-molten globule state": four-state guanidinium chloride-induced unfolding of carbonic anhydrase B at low temperature. *J. Mol. Biol.* **255**, 215–228.
78. Uversky, V. N. & Ptitsyn, O. B. (1994). "Partly folded" state, a new equilibrium state of protein molecules: four-state guanidinium chloride-induced unfolding of β-lactamase at low temperature. *Biochemistry*, **33**, 2782–2791.
79. Gualfetti, P. J., Iwakura, M., Lee, J. C., Kihara, H., Bilsel, O., Zitzewitz, J. A. & Matthews, C. R. (1999).

Apparent radii of the native, stable intermediates and unfolded conformers of the α-subunit of tryptophan synthase from *E. coli*, a TIM barrel protein. *Biochemistry*, **38**, 13367–13378.
80. Saab-Rincon, G., Gualfetti, P. J. & Matthews, C. R. (1996). Mutagenic and thermodynamic analyses of residual structure in the α subunit of tryptophan synthase. *Biochemistry*, **35**, 1988–1994.
81. Blaustein, R. O. & Finkelstein, A. (1990). Voltage-dependent block of anthrax toxin channels in planar phospholipid bilayer membranes by symmetric tetraalkylammonium ions. Effects on macroscopic conductance. *J. Gen. Physiol.* **96**, 905–919.
82. Murzin, A. G., Lesk, A. M. & Chothia, C. (1994). Principles determining the structure of β-sheet barrels in proteins. I. A theoretical analysis. *J. Mol. Biol.* **236**, 1369–1381.
83. Oomen, C. J., Van Ulsen, P., Van Gelder, P., Feijen, M., Tommassen, J. & Gros, P. (2004). Structure of the translocator domain of a bacterial autotransporter. *EMBO J.* **23**, 1257–1266.
84. Krimm, S. & Tiffany, M. L. (1974). The circular dichroism spectrum and structure of unordered polypeptides and proteins. *Isr. J. Chem.* **12**, 189–200.
85. Wilson, G., Hecht, L. & Barron, L. D. (1996). Residual structure in unfolded proteins revealed by Raman optical activity. *Biochemistry*, **35**, 12518–12525.
86. Shi, Z., Woody, R. W. & Kallenbach, N. R. (2002). Is polyproline II a major backbone conformation in unfolded proteins? *Advan. Protein Chem.* **62**, 163–240.
87. Wimley, W. C. (2002). Toward genomic identification of β-barrel membrane proteins: composition and architecture of known structures. *Protein Sci.* **11**, 301–312.
88. Buck, M. (1998). Trifluorethanol and colleagues: cosolvents come of age. Recent studies with peptides and proteins. *Quart. Rev. Biophys.* **31**, 297–355.
89. Kentsis, A. & Sosnick, T. R. (1998). Trifluoroethanol promotes helix formation by destabilizing backbone exposure: desolvation rather than native hydrogen bonding defines the kinetic pathway of dimeric coiled coil folding. *Biochemistry*, **37**, 14613–14622.
90. Conio, G., Patrone, E. & Brighetti, S. (1970). The effect of aliphatic alcohols on the helix-coil transition of poly-L-ornithine and poly-L-glutamic acid. *J. Biol. Chem.* **245**, 3335–3340.
91. Krantz, B. A., Moran, L. B., Kentsis, A. & Sosnick, T. R. (2000). D/H amide kinetic isotope effects reveal when hydrogen bonds form during protein folding. *Nature Struct. Biol.* **7**, 62–71.
92. Krantz, B. A., Srivastava, A. K., Nauli, S., Baker, D., Sauer, R. T. & Sosnick, T. R. (2002). Understanding protein hydrogen bond formation with kinetic H/D amide isotope effects. *Nature Struct. Biol.* **9**, 458–463.
93. Barnard, A., Jr & Payton, M. (1995). Fermentation and growth of *Escherichia coli* for optimal protein production. In *Current Protocols in Protein Science* (Coligan, J.E., Dunn, B.M., Plough, H.L., Speicher, D.W. & Wingfield, P.T., eds), pp 1–18, Chapt. 5.3 Wiley.
94. Fraczkiewicz, R. & Braun, W. (1998). Exact and efficient analytical calculation of the accessible surface areas and their gradients for macromolecules. *J. Comput. Chem.* **19**, 319–333.
95. Guex, N. & Peitsch, M. C. (1997). Swiss-Model and the Swiss-PdbViewer: an environment for comparative protein modeling. *Electrophoresis*, **18**, 2714–2723.
96. Richards, F. M. (1974). The interpretation of protein structures: total volume, group volume distributions and packing density. *J. Mol. Biol.* **82**, 1–14.

Edited by G. von Heijne

(Received 9 August 2004; received in revised form 22 September 2004; accepted 23 September 2004)